Towards High-Resolution Ultrasound Neuromodulation With Crossed-Beam Phased Arrays

Sheikh Jawad Ilham, *Student Member, IEEE*, and Mehdi Kiani, *Senior Member, IEEE*

***Abstract*—Transcranial focused ultrasound stimulation (tFUS) has emerged as a potential noninvasive therapeutic technology. Due to skull attenuations at high ultrasound (US) frequencies, successful tFUS with sufficient penetration depth requires sub-MHz US waves, leading to relatively poor stimulation specificity particularly in the axial direction (perpendicular to the US transducer). This shortcoming can potentially be overcome by utilizing two individual US beams properly crossed in time and space. For large-scale tFUS, a phased array is also required to dynamically steer focused US beams at desired neural targets. This article presents the theoretical foundation and optimization (through a wave-propagation simulator) of crossed-beam formation using two US phased arrays. It also experimentally validates crossed-beam formation with two custom-made 32-element phased arrays (operating at 555.5 kHz) positioned relatively at different angles. In measurements, the sub-MHz crossed-beam phased arrays achieved 0.8/3.4 mm lateral/axial resolution at a focal distance of ∼ 46 mm, compared to the lateral/axial resolution of 3.4/26.8 mm of the individual phased array at 50 mm focal distance (∼ 28.4-fold improvement in reducing the main focal zone area). The crossed-beam formation in the presence of a rat skull and a tissue layer was also validated in the measurements.**

***Index Terms*—Ultrasound, crossed beam, phased array, transducer, high resolution, transcranial, neuromodulation.**

I. Introduction

LOW-INTENSITY transcranial focused ultrasound stimulation (tFUS) has emerged as a therapeutic alternative to the established noninvasive neuromodulation technologies, such as transcranial magnetic stimulation as well as transcranial direct and alternating current stimulation [1]. The tFUS has experimentally been effective in evoking and/or suppressing various neural responses in different animal models in numerous studies [2], [3], [4], [5], [6], [7], [8], [9], [10]. More recently, the potential of tFUS in treating various neural, neuronal, and neurodegenerative conditions in humans have also been demonstrated [11], [12], [13], [14], [15], [16], [17].

Manuscript received 10 February 2023; revised 21 April 2023; accepted 8 June 2023. Date of publication 13 June 2023; date of current version 12 July 2023. This work was supported by the National Science Foundation under Grants ECCS-1942839 and ECCS-2143557. This paper was recommended by Associate Editor D. Hall. *(Corresponding author: Mehdi Kiani.)*

The authors are with the School of Electrical Engineering and Computer Science, Pennsylvania State University, University Park, PA 16802 USA (e-mail: sjl6090@psu.edu; mkiani@psu.edu).

Color versions of one or more figures in this article are available at https://doi.org/10.1109/TBCAS.2023.3285724.

Digital Object Identifier 10.1109/TBCAS.2023.3285724

The tFUS is superior to its noninvasive counterparts due to its relatively finer spatial resolution, higher penetration depth, and larger spatial coverage thanks to focused ultrasound (US) beams that can also be steered and targeted electronically using phased arrays [18], [19], [20], [21]. While the US loss in the soft tissue is as low as ∼ 0.5-1 dB/MHz/cm, its attenuation in the skull is much higher (∼ 15 dB/MHz/cm) [22]. Therefore, to achieve sufficient penetration depth while minimizing the reflection, scattering, absorption, and unwanted aberrations from the skull, most conventional tFUS systems require and operate with US beams at sub-MHz sonication frequencies ($f < 1$ MHz) [23].

Operating at low frequencies drastically degrades the spatial resolution of the US beam specifically in the axial direction (perpendicular to the US transducer), leading to a poor stimulation specificity as evident in many prior works such as [7], [8], [9], [14], [15]. In these works, the tFUS in $f = 250$–600 kHz range has successfully been implemented in various animal models, where the lateral and axial resolutions of the US beams generated by single-element transducers vary from 3 mm to 4.9 mm and 11.5 mm to 47 mm, respectively (at focal distances ranging from 10 mm to 30 mm). For instance, the tFUS system in [15] that modulates the primary somatosensory cortex activity in humans operates at $f = 500$ kHz, resulting in an acoustic beam with the lateral/axial spatial resolution of 4.9/18 mm at a 30 mm focal depth.

The lateral (parallel to the US transducer) and axial (normal to the US transducer) spatial resolution is defined as the beam width at which the US intensity reduces to half (−3 dB) or the US pressure reduces by ∼1.4-fold [23]. The poor spatial resolution in the aforementioned tFUS works, particularly in the axial direction, is partly due to the low frequency operation and use of non-focused single-element transducers. For transducers with a large f-number, defined as the ratio of the focal depth to the transducer aperture, the beam width along the axial direction (scaled by the f-number squared) is often larger than that along the lateral direction (scaled linearly with the f-number) [24].

A focused transducer in the form of a single-element transducer with a lens (or curvature) or a US phased array can improve the spatial resolution even at low frequencies. In [5], beam focusing with an 800 kHz single-element transducer has been achieved by pressing a steel ball onto the piezoelectric composite during fabrication (creating a curved surface) and adding an external collimator. In [25], a comprehensive study

of single-element transducers with different characteristics has been provided, demonstrating that adding a focusing lens on the front surface of a transducer significantly improves the spatial resolution, particularly in the lateral direction.

A US phased array can electronically be driven in a beamforming manner to focus and steer US beams towards different neural targets. In [26], we have proposed a detailed methodology for the design and optimization of US arrays for tFUS applications. A 16-element linear array was designed and fabricated at $f =$ 833.3 kHz, achieving measured lateral/axial beam resolution of 1.6/9 mm at a 12 mm focal depth. Several other US phased arrays have also been reported for the tFUS, including the ring-shaped 32-element capacitive micro-machined US transducer (CMUT) array ($f =$ 183 kHz) in [18] with 2.75 mm lateral resolution at 2.3 mm focal depth; 5 MHz linear 128-element piezoelectric US array in [19] with 1.77 mm lateral resolution; the 2D transmit beamformer ASIC with integrated 8.4 MHz, 26×26-element piezoelectric transducers with $\sim$ 0.2/1.68 mm lateral/axial resolution at 5 mm focal depth in [20]; and the 2D transmit beamformer CMOS ASIC with the integrated 2 MHz, 32×32-element CMUT array in [21] with 0.4/2.4 mm lateral/axial resolution at 5 mm focal depth.

In both [20] and [21], the spatial resolution has significantly been improved by focusing beams at a short distance and operating at high $f \geq 2$ MHz, both of which are not optimal for tFUS in large animals and humans with thick skulls and large brains. It is also worth noting that the axial beam width in these high frequency arrays is still much larger than the lateral beam width. To mitigate this and achieve a focused beam in a confined volume at a large focal depth, a beam intersection technique that aggregates multiple 2D arrays and directs their beams to the far field has been proposed in [21], although its implementation has not been demonstrated yet.

The spatial resolution of the US beam generated by sub-MHz transducers in tFUS applications can further be improved by utilizing the concept of crossed-beam formation. Crossing two individual US beams (generated by two separate transducers) properly can result in a composite beam with significantly improved axial resolution and higher spatial peak pressure. In [27], two 5 MHz US beams generated by a pair of focused single-element transducers have been crossed orthogonally to improve the axial resolution from 11 mm (one beam) to 1.1 mm (crossed beam) at 38.1 mm focal depth. But mechanical movement of the single-element transducers in [27] is required for the crossed-beam formation at different targets, which eventually makes this technology impractical for the use in large-scale tFUS in freely behaving subjects. Although, some limited beam crossing analysis with single-element transducers has been provided in [27], the literature lacks a detailed study of optimal beam crossing particularly using US phased arrays with the focusing/steering capability for large scale tFUS.

This article presents the theory, optimization (through a wave-propagation simulator), and experimental validation of the crossed-beam formation using two phased arrays for large-scale tFUS applications. As shown in Fig. 1, both the spatial resolution and coverage of a tFUS system can radically be improved by optimizing and implementing the beam crossing condition using

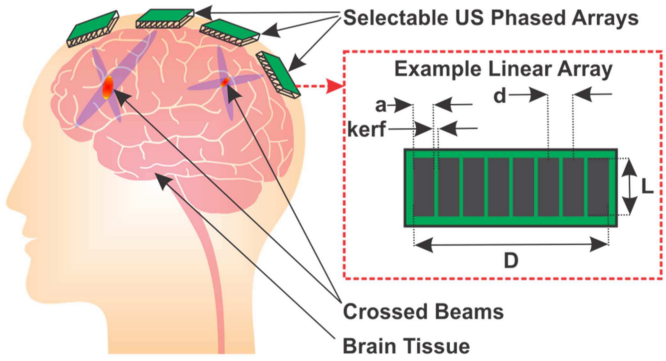

Fig. 1. Conceptual diagram of proposed crossed-beam method with selectable US phased arrays for the tFUS with high spatial resolution and coverage.

US phased arrays (in general could be multiple selectable 1D or 2D arrays). Crossing two US beams is a complex wave interference phenomenon, requiring accurate analysis of crossed-beam characteristics. This work has several contributions: 1) Exploring the theoretical foundation of the crossed-beam formation by crossing two individual US beams; 2) Presenting detailed methods for the optimization of beam crossing and development of a framework using a wave propagator simulator; 3) Experimentally demonstrating the crossed-beam formation using two US phased arrays and validating it with different propagation media.

The theoretical aspects of the crossed-beam formation by crossing two US beams will be discussed in Section II, including the optimization of beam crossing with phased arrays. Section III will summarize the fabrication of the prototype US phased arrays, implementation of the beam crossing with two arrays, and measurement results. Section IV will discuss the practicality of the crossed-beam formation using phased arrays, followed by the concluding remarks in Section V.

II. Crossed Ultrasound Beams Generated by Phased Arrays for High-Resolution tFUS

A. Theory of Interference of Two Ultrasound Beams

Interference of two or more coherent plane waves abides by the principle of linear superposition, which was first demonstrated by Thomas Young with the famous double slit experiment back in 1802 [28]. When a focused (physically curved) single-element transducer is driven at a particular frequency, its distributed point sources having constant phase relations act like coherent wave sources. Thus, according to the principle of interference, a focused transducer can generate a particular interference pattern, which is termed as a beam as shown in Fig. 2(a) (left). Similarly, when the elements of a US phased array are driven at a particular frequency with a certain delay pattern, they maintain a constant phase relation acting like coherent wave sources. Therefore, a beam is formed according to the principle of interference as shown in Fig. 2(b) (left).

The principle of interference is also applicable in the case of forming a crossed beam, such as interference of more than one beam generated by multiple focused single-element transducers

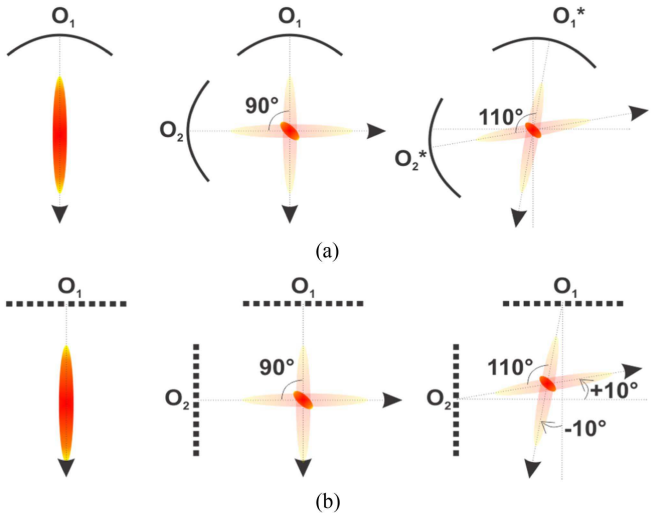

Fig. 2. Conceptual diagrams of crossed-beam formation by using focused single-element and phased-array transducers. (a) A focused beam generated by a curved single-element transducer and two identical beams crossed at 90° and 110° angles. (b) A focused beam generated by a phased array and two identical arrays for crossing their corresponding beams at 90° and 110° angles.

(Fig. 2(a)) or phased arrays (Fig. 2(b)) all driven at an identical frequency. Fig. 2(a) shows two identical beams generated by two orthogonally positioned curved single-element transducers, in which the beams are crossed at 90° and 110° angles. For a 110° crossing, the transducers must be moved mechanically. Fig. 2(b) shows two orthogonally positioned identical phased arrays and the crossing of their corresponding beams at 90° and 110° angles. Compared to single-element transducers, phased arrays can cross beams at angles other than 90° (e.g., 110° in Fig. 2(b)) by electronically steering focused beams (e.g., −10° and 10° in Fig. 2(b)) without the need for any mechanical movements. In other words, the crossed-beam formation can be achieved at different targets by steering beams at different angles.

To exploit a crossed beam in enabling high-resolution tFUS, its formation and characteristics need to be investigated. Due to its complexity, the US pressure distribution (beam profile) of a crossed beam formed at any arbitrary angles and locations can be estimated using wave propagator simulators, such as the k-Wave toolbox of the MATLAB (MathWorks R2019b, Natick, MA). To explore the crossed-beam method for the tFUS, two research questions will be addressed in this section. 1) Is it possible to form a crossed beam anywhere in a given medium using two individual beams? 2) What is the optimum condition for crossing two beams to achieve high spatial resolution and high US pressure output? For single-element transducers with a fixed beam profile, the optimum crossing conditions comprise of the crossing angle and the crossing location on the beams. Whereas for phased arrays, which generate different beam profiles when focusing/steering beams at various depths/angles, the optimum crossing conditions include the steering angles (related to the crossing angle) and the focal depth (related to the crossing location on the beams) of the individual arrays.

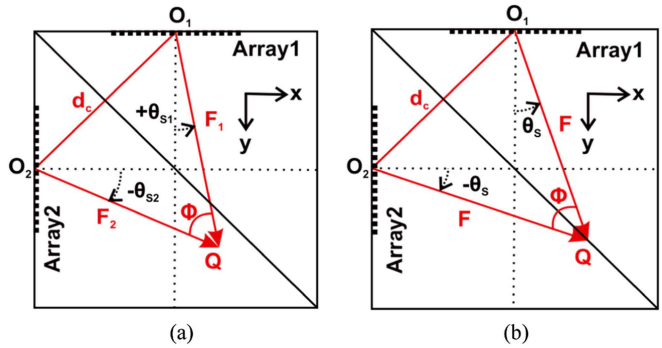

Fig. 3. Beam crossing scenarios with two phased arrays. (a) General case, where targeted crossing point Q could be anywhere in a 2D plane. (b) A particular case, where Q is located on the perpendicular bisector of line O_1O_2.

B. Optimal Crossed-Beam Formation

Let's assume a scenario where two phased arrays are centered at the points O_1 $(\boldsymbol{x_{o1}}, \boldsymbol{y_{o1}})$ and O_2 $(\boldsymbol{x_{o2}}, \boldsymbol{y_{o2}})$ of a 2D cartesian grid, as shown in Fig. 3(a). If a crossed beam is intended to be formed at any arbitrary point Q $(\boldsymbol{x_q}, \boldsymbol{y_q})$, the individual beams of the arrays need to cross each other properly in both time and space. In other words, all the US waves generated by the individual elements of the two arrays should simultaneously reach at point Q. With the known coordinates of the arrays' center and the targeted crossing point, the distances from the respective arrays' center to the beam crossing point (F_1 and F_2) and the corresponding steering angles (θ_{S1} and θ_{S2}), as shown in Fig. 3, can be calculated using simple coordinate geometries.

$$F_1 = \sqrt{(x_q - x_{01})^2 + (y_q - y_{o1})^2} \tag{1}$$

$$F_2 = \sqrt{(x_q - x_{02})^2 + (y_q - y_{o2})^2} \tag{2}$$

$$\theta_{S1} = \tan^{-1}\left(x_q/\left(y_q + y_{o1}\right)\right) \tag{3}$$

$$\theta_{S2} = \tan^{-1}\left(y_q/(x_q + x_{o2})\right) \tag{4}$$

Then, the corresponding delay patterns for each of the arrays can be obtained from [26],

$$\Delta t_n = (F/c)\left(1 - \sqrt{\left[1 + (nd/F)^2 - 2ndsin\left(\theta_s\right)/F\right]}\right) + t_0, \tag{5}$$

where d is the interelement spacing (Fig. 1 inset), F is the focal distance, θ_s is the steering angle, Δt_n is the excitation time delay for the n^{th} array element, c is the US velocity in the medium, and t_0 is a common delay offset for all the elements. By driving the arrays using the delay patterns in (5), a crossed beam different from the individual beams can be formed. This guarantees the formation of a crossed beam with an improved axial resolution. But the characteristics of the crossed beam vary based on the crossing angles of the beams as well as the crossing locations on the beams. To accurately model the crossed beam, the k-Wave toolbox is used that numerically calculates the resultant acoustic field radiated from multiple sources by solving a set of

coupled first-order wave equations. The k-Wave accuracy has experimentally been validated [29].

Although the above-mentioned method in Fig. 3(a) represents a general case of beam crossing, for the sake of simplicity in studying the effect of the crossing angle and location, a particular case shown in Fig. 3(b) where the beam crossing occurs on the perpendicular bisector of the line connecting the centers of the arrays O_1, O_2 is considered. For this simpler case in Fig. 3(b), $F_1 = F_2 = F$ and $|\theta_{S1}| = |\theta_{S2}| = \theta_S$ that results in the arrays' center-to-center distance (d_C) of

$$d_C = \sqrt{2}F\,[\cos(\theta_S) + \sin(\theta_S)]. \tag{6}$$

In this case, the crossing angle is $\Phi = 90° + 2\theta_S$, which can theoretically vary in the range of $0° < \Phi < 180°$ with the steering angle of $-45° < \theta_S < 45°$.

A method is proposed here to find out Φ and location on the beam that result in the optimum crossed-beam formation. For simplicity in k-Wave simulations, the following assumptions are made. 1) The arrays are simplified with two focused single-element transducers with identical radius of curvature and diameter (aperture). Thus, the generated beams by both transducers are identical in terms of their beam profile. 2) To model the effect of the crossing location on each beam while keeping Φ constant, the transducers are moved with respect to the crossing point O, which is fixed at the center of the defined 2D grid. 3) To model different Φ scenarios while keeping F constant, the transducers are moved along a circle around the crossing point (in other words, different segments of a circle are considered as transducers).

The sequential steps for the k-Wave simulation setup are as follows. As shown in Fig. 4(a), a 2D k-grid is defined in the k-Wave and a curved transducer is built. The generated beam by the transducer is simulated, from which the distance between the transducer center to the maximum US pressure point is calculated (Fig. 4(a) left). This is the initial value of the crossing location on the beam. The position of the transducer is changed such that the maximum peak pressure point is right in the center of the plane, i.e., the origin O of the defined kgrid (Fig. 4(a) right). The origin is also used to identify a circle with a radius equal to the radius of the transducer curvature, acting like the host of the two identical curved transducers with the same distance to the origin, as shown in Fig. 4(b) and (c). Selecting different segments of this circle as two transducers can provide two beams crossed at different crossing angles Φ.

Fig. 4(b) implements two transducers with beam crossing at $\Phi = 90°$. The US beam profiles in Fig. 4(b) show the effect of changing the crossing location on the beam simply by shifting the center position of the transducers with respect to the origin (note that this changes d_C). The transducers' arrangement on the left plot clearly shows a better beam crossing scenario (i.e., smaller focal area). Comparing the beams in Fig. 4(a) and (b) indicates that the focal spot of the crossed-beam profile is much smaller than that of the single beam (axial resolution of ~ 6 mm vs. 50 mm). Fig. 4(c) shows the effect of changing Φ from 90° (left) to 120° (right) on the resultant crossed-beam profile.

To find the optimal crossing condition, a metrics is needed for the quantitative comparison of different cases. As discussed

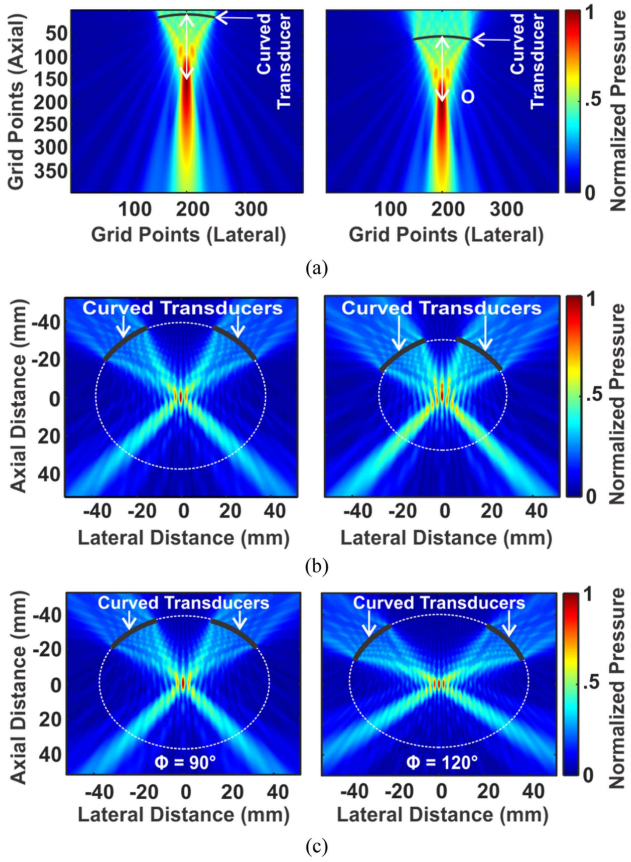

Fig. 4. Simplifying phased arrays with curved transducers in k-Wave to study the effect of crossing angle (Φ) and crossing location on a beam. (a) Identifying the maximum US pressure point on the beam and moving it to the origin O of the grid. (b) Crossing two beams at two different beam locations for the same Φ of 90°. (c) Crossing two beams at two different angles (left: $\Phi = 90°$; right: $\Phi = 120°$) but at the same beam locations.

in [26], a balance between the power efficiency and spatial resolution of the tFUS system is required to ensure achieving sufficient US pressure at the target with the smallest focal spot (better specificity) and the least amount of input electrical power. Thus, a figure of merit, $FoM = P_{max}/\sqrt{A_{beam}}$, is defined as the ratio of the maximum US pressure, P_{max}, to the square root of the half-power beam area, A_{beam}, at the focal spot.

Fig. 5 shows the effect of the crossing location and angle (Φ) on the profile of the formed crossed beam, quantified with the normalized P_{max}, A_{beam} (area where pressure $> \sim 0.71$), and defined FoM. In Fig. 5(a), while keeping Φ fixed at 90°, the location of the beam crossing has been swept (similar to Fig. 4(b)). It shows that the finest spatial resolution (smallest A_{beam}) and the highest FoM are achieved at ~ 45 mm away from the transducers' center (P_{max} is fairly constant at different crossing locations). Keeping the crossing location fixed at ~ 45 mm from the transducers, Φ was swept from 50° to 110° that led to the optimum Φ of 70°, minimizing A_{beam} and maximizing FoM. The crossing location and angle should be swept iteratively to achieve the most optimum crossing conditions.

To further extend these results, the optimum Φ was found in a similar iterative process for various beams (with different beam profiles) generated by single-element curved transducers with

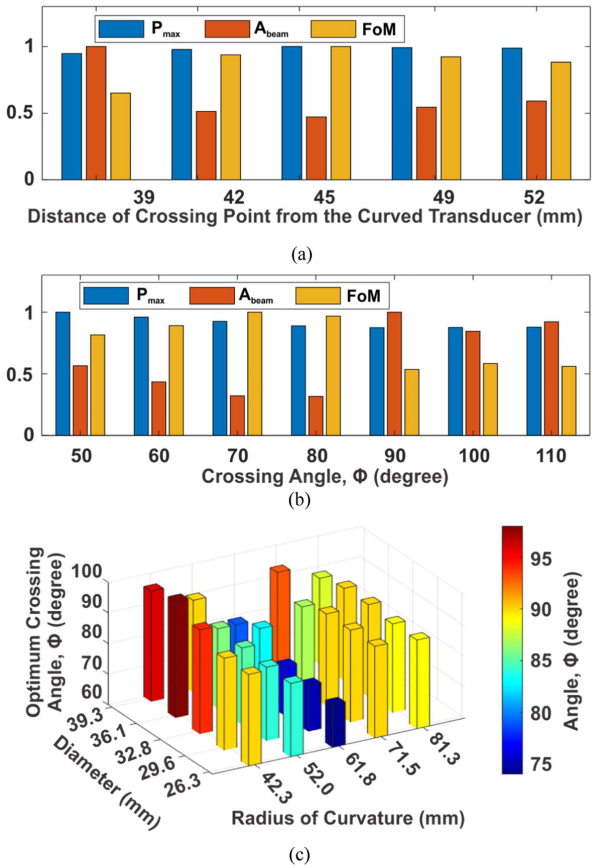

Fig. 5. Normalized crossed-beam properties (maximum pressure, P_{max}, half-power beam area, A_{beam}, and FoM) for (a) sweeping the crossing point distance from the curved transducer center with $\Phi = 90°$ and (b) optimization of Φ while crossing at optimum beam location for one beam profile. (c) 3D plot of optimum Φ for various beam profiles generated by different radius of the curvature and diameter of single-element curved transducers.

different radius of curvature and diameter. Fig. 5(c) represents the optimum Φ for crossing 25 different beams for various radius of curvature of 42.25-81.25 mm and diameter of 26.32-39.32 mm. From these simulations, a few observations can be made on the optimal crossing conditions. 1) The optimum location of the crossing on a beam depends on the relative position of the peak US pressure area in a beam, or alternatively the pattern of the pressure distribution of a particular beam. 2) The beam profile changes aggressively with the radius of the curvature and so does the optimum Φ. 3) The beam profile changes slightly with the diameter (or aperture), and therefore, the optimum Φ is slightly different when the diameter changes. Note that the curved transducers in these simulations are mechanically moved for crossing at different beam locations. Therefore, the beam profile remains constant for the same transducer geometry. However, the beams generated by a phased array may vary in shape and pressure distribution/level while being focused and steered at different distances and angles [26].

C. Crossed-Beam Formation with Two Phased Arrays

To form a crossed beam using two phased arrays, the following valid assumptions are made. 1) The arrays are fixed at their respective positions, i.e., d_C is fixed. 2) For optimum beam crossing, individual beams are formed at different focal distances (F) and/or steering angles (θ_S) by electronically changing the excitation delays based on (5). 3) Depending on F and/or θ_S, the US profile of each individual beam (with an elliptical shape) may vary. Therefore, both crossing location and angle can potentially change with various F and θ_S, needed for targeting at different locations.

TABLE I
OPTIMIZED ARRAY SPECIFICATIONS FOR CROSSED-BEAM SIMULATIONS AND MEASUREMENTS

Parameters	Optimized US Array	Fabricated US Array
Sonication Frequency, f (kHz)	500	555.55
Target Focal Distance, F (mm)	50	50
Number of US Elements, N	32	32
US Array Aperture, D (mm)	49.7	~ 50
US Element Length, L (mm)	19.5	20.5
US Element Width, a (mm)	1.3	~ 1.4
US Interelement Spacing, d (mm)	1.56	~ 1.56
Steering Angle, θ_s (deg)	±60	±60
Kerf, *kerf* (mm)	0.26	~ 0.16

While (1)–(4) can provide the required $[F_1, \theta_{S1}]$ and $[F_2, \theta_{S2}]$ of each array for focusing each individual beam at the desired location Q (x_q, y_q), an optimization around these initial geometrically calculated values is needed (due to the beam profile variations) to find the optimum crossing condition that maximizes the FoM. For simplicity, the particular case in Fig. 3(b) is studied with $F_1 = F_2 = F$ and $|\theta_{S1}| = |\theta_{S2}| = \theta_S$. For the optimization, two identical 32-element arrays (operating at 500 kHz and orthogonally positioned with a d_C of ~ 71 mm) with an aperture (D) of ~ 50 mm are modeled and simulated in the k- Wave. The array specifications are summarized in Table I.

Fig. 6 demonstrates the process of accurately finding the optimum F (for optimal crossing location on the beam) for three different crossing angles of $\Phi = 70°$ ($\theta_{S1} = 10°$, $\theta_{S2} = -10°$), $\Phi = 90°$ ($\theta_{S1} = \theta_{S2} = 0°$), and $\Phi = 120°$ ($\theta_{S1} = -15°$, $\theta_{S2} = 15°$). For $\Phi = 70°$, the optimum F was found to be ~ 45 mm (Fig. 6(a)), improving the FoM by ~ 3.5-fold compared to the FoM of the geometrically calculated F of ~ 62 mm based on (6) with $d_C = 71$ mm, $\theta_{S1} = 10°$, and $\theta_{S2} = -10°$. In Fig. 6(b) for $\Phi = 90°$, the optimum F that increased the FoM by 12.5-fold was ~ 35 mm (different from its initial value of ~ 50 mm). Similarly, for $\Phi = 120°$ the optimum F was found to be ~ 30 mm (Fig. 6(c)), F of ~ improving FoM by ~ 13-fold compared to that with the initial 41 mm. These results imply that a lower crossing angle (Φ) can tolerate a larger margin of error in forming a proper crossed beam with high FoM. Overall, these examples in Fig. 6 justify the necessity for the optimization.

Fig. 7 compares the simulated 2D US beam profiles of the individual array (top row) with the crossed-beam profiles of the orthogonally positioned arrays (bottom row) at the optimum crossing conditions (optimum F) for three different Φ of 70° (Fig. 7(a)), 90° (Fig. 7(b)), and 120° (Fig. 7(c)). The crossed beam at $\Phi = 90°$ ($\theta_S = 0°$) in Fig. 7(b) achieves the lateral/axial resolution of 1.1/2.9 mm with an A_{beam} of 2.1 mm^2. This is a 10.5-fold improvement in A_{beam} compared to $A_{beam} = 22$ mm^2

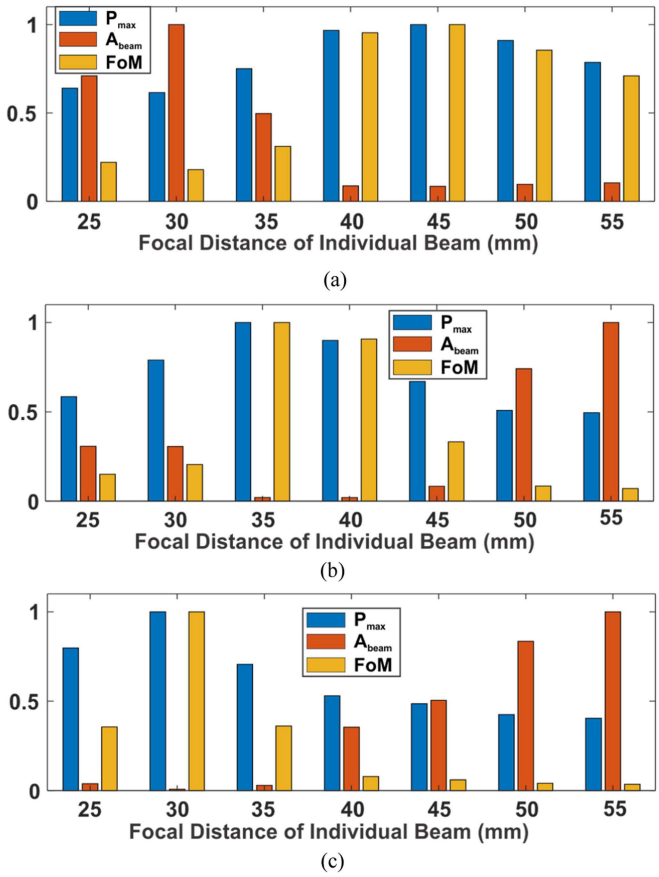

Fig. 6. Optimization of individual array focal distance F for optimal beam crossing at three different conditions of (a) $\Phi = 70°$ ($\theta_{S1} = 10°$, $\theta_{S2} = -10°$), (b) $\Phi = 90°$ ($\theta_{S1,2} = 0°$), and (c) $\Phi = 120°$ ($\theta_{S1} = -15°$, $\theta_{S2} = 15°$).

of the single beam (Fig. 7(b) top) with the lateral/axial resolution of 2.6/13.8 mm. Fig. 7(a) and (c) show the beam profiles for optimum beam crossing at $\Phi = 70°$ ($\theta_{S1} = 10°, \theta_{S2} = -10°$) and $\Phi = 120°$ ($\theta_{S1} = -15°, \theta_{S2} = 15°$), resulting in the lateral/axial resolution of 1.1/4 mm ($A_{beam} = 3.6$ mm^2) and 0.7/2.6 mm ($A_{beam} = 1.4$ mm^2), respectively. Both results show a significant improvement in reducing A_{beam} compared to the single beam. All the US pressure values in Fig. 7 are normalized to the peak US pressure of the crossed beam at $\Phi = 90°$ (Fig. 7(b): bottom). Thus, in addition to the spatial resolution improvement, the peak US pressure of the crossed beam is almost doubled compared to the single beam.

Additionally, to analyze the feasibility of crossed-beam formation by two coplanar phased arrays (which is not possible using single-element transducers), the two 32-element arrays were positioned side by side with no separation (d_C of ~ 50 mm; Fig. 8(a)) and 21 mm separation (d_C of ~ 71 mm; Fig. 8(b)). The optimal conditions for the crossed-beam formation at an axial distance of ~ 35 mm in the middle of the arrays (similar condition to the single array and orthogonal arrays in Fig. 7(b) were found in simulations. The crossed-beam profiles in Fig. 8(a) and (b) indicate the lateral/axial resolution of 1.37/5.85 mm ($A_{beam} = 6.16$ mm^2) and 0.98/5.66 mm ($A_{beam} = 4.5$ mm^2) for arrays' separation of 0 and 21 mm, respectively.

Although the crossed beams generated by the coplanar arrays are significantly improved compared to the single beam (Fig. 7(b): top), the orthogonally positioned arrays (Fig. 7(b): bottom) with crossed beams still achieve much better resolution (1.1/2.9 mm lateral/axial resolution; $A_{beam} = 2.1$ mm^2). Also, such coplanar arrangement constrains the crossed-beam formation within an area/volume only in the middle of the arrays, as steering a beam laterally far away from an array requires a very large θ_S, which is even impractical (and not optimal) in some conditions. Nonetheless, these simulations with different relative angles of arrays show the significance of beam crossing using phased arrays with beam focusing/steering capability that can be achieved with different arrays' arrangement (unlike single-element transducers).

III. Measurement Results

A. Array Design, Fabrication, and Characterization

To validate the crossed-beam formation with phased arrays, two identical arrays were designed and fabricated following our optimization and fabrication procedures described in [26]. For the array optimization, the following assumptions were made in k-Wave simulations. 1) For tFUS application, f is mostly considered well below 1 MHz to reduce US attenuation in skull that led us to choose $f = 500$ kHz. 2) The maximum number of elements (N) was considered to be 32 since we had access to commercially available 32-channel beamforming electronics. 3) To demonstrate focusing beams at large distances (suitable for deep tissues) and facilitate crossed-beam measurements, the targeted F was set to 50 mm with $\pm 60°$ beam-steering capability (maximum θ_S). 4) As described in [26], an equivalent directivity function $H(y)$, which is defined as the ratio of the peak US pressure output along the lines perpendicular to the array to the peak US pressure output at the focal spot, was set to < 0.5 to minimize the side/grating lobes. The thickness of each element was optimized in the COMSOL Multiphysics (COMSOL, Inc., Bulington, MA) to resonate them at $f = 500$ kHz. The dimensions of the optimized linear array (Fig. 1 inset) are aperture D of 49.7 mm, element length (L) of 19.5 mm, element width (a) of 1.3 mm, and interelement spacing (d) of 1.56 mm.

Following the detailed fabrication procedure in [26], two 32-element arrays were fabricated by dicing a bulk PZT (APC-840) plate, which was electrically/mechanically secured on a printed circuit board (PCB), and wire bonding its top plates to the excitation pads, as shown in Fig. 9(a) [26]. Since a ~ 160 μm thick saw blade was available to us, the fabricated $a = 1.4$ mm was slightly larger than the optimized a. For the electrical isolation and protection of the wire bonds, a layer of sylgard-184 (Dow Inc., Midland, MI) was coated on the assembled devices. Table I summarizes the specifications of the fabricated arrays.

The impedance of each element in the fabricated arrays (Array-1 and Array-2) was first measured at different frequencies. Fig. 9(b) and (c) show the impedance ensemble plots of all the 32 elements of two arrays with a series resonance in a frequency range of 500–600 kHz. Thus, $f = 555.55$ kHz was chosen as the driving frequency for performing all the subsequent measurements (also considering the driver configuration).

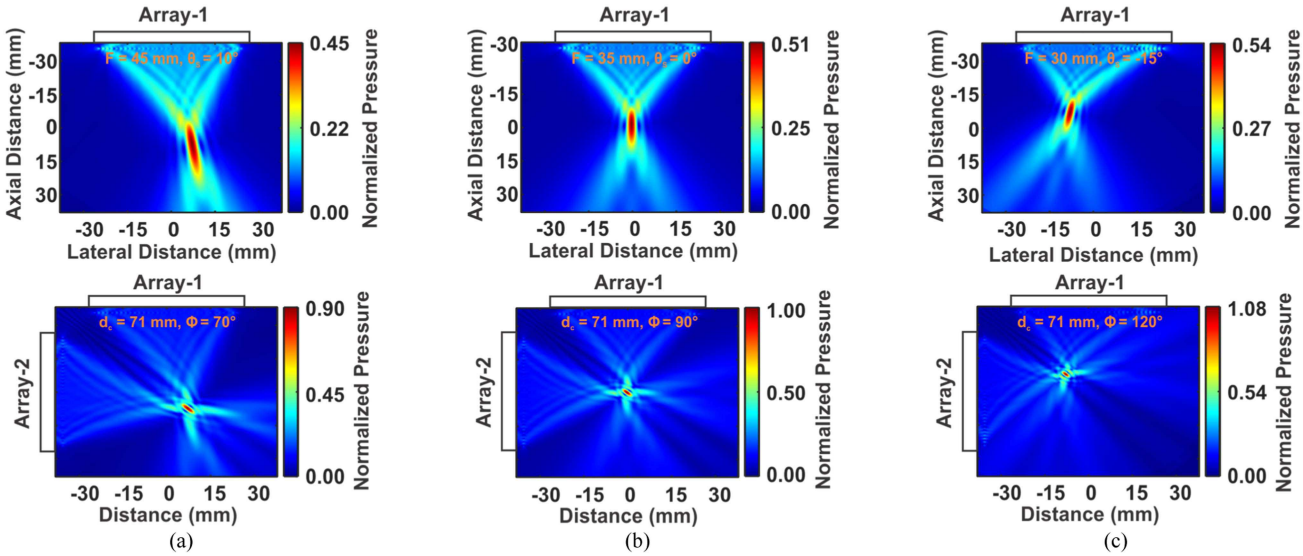

Fig. 7. Simulated 2D beam profiles (pressure distribution) of the individual array (top row) and crossed-beam arrays (bottom row) at optimum focal distances of $F = 45$ mm, 35 mm, and 30 mm for crossing at (a) $\Phi = 70°$ ($\theta_{S1} = 10°$, $\theta_{S2} = -10°$), (b) $\Phi = 90°$ ($\theta_{S1,2} = 0°$), and (c) $\Phi = 120°$ ($\theta_{S1} = -15°$, $\theta_{S2} = 15°$), respectively. All the pressure values are normalized to the maximum pressure recorded in the orthogonal ($\Phi = 90°$) crossed-beam profile.

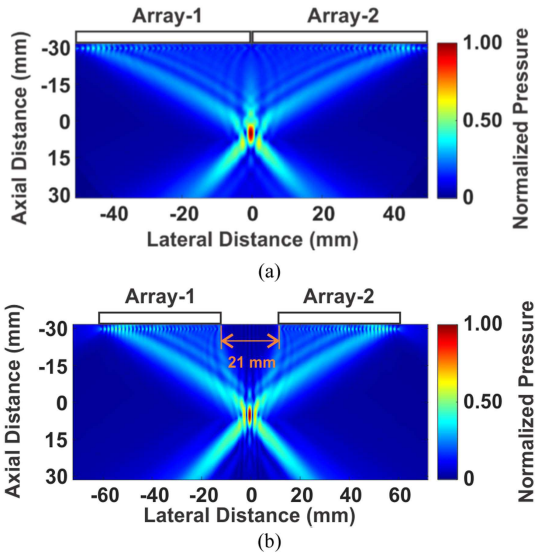

Fig. 8. Simulated crossed-beam profiles of two coplanar 32-element arrays placed side by side with the separation of (a) 0 mm ($d_C = 50$ mm) and (b) 21 mm ($d_C = 71$ mm) for beam formation at ~ 35 mm axial distance.

At $f = 555.55$ kHz, the elements' impedance was within the range of 0.84-1.2 kΩ and 0.94-1.1 kΩ for Array-1 and Array-2, respectively (excluding two edge elements).

The individual arrays were also comprehensively tested to verify their capability in beam focusing and steering. For these measurements, a commercially available TX7332EVM board (Texas Instruments, Dallas, TX) with 32 channels of high-voltage drivers (up to 150 V peak to peak) and a delay range of 0-40 μs with 5 ns resolution was used. An accurate experimental setup (similar to the setup in [26]) was used to characterize the arrays in a water tank.

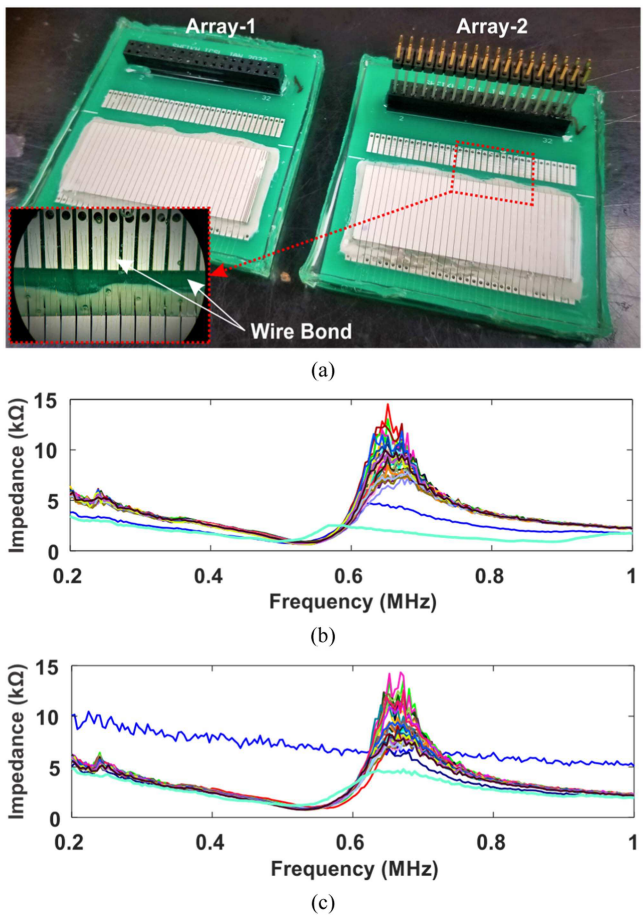

Fig. 9. (a) Images of two fabricated arrays (wire-bonds shown inset) for crossed-beam measurements. (b) and (c) Measured impedance of all 32 elements in the first and second array within a frequency range of 0.2-1 MHz.

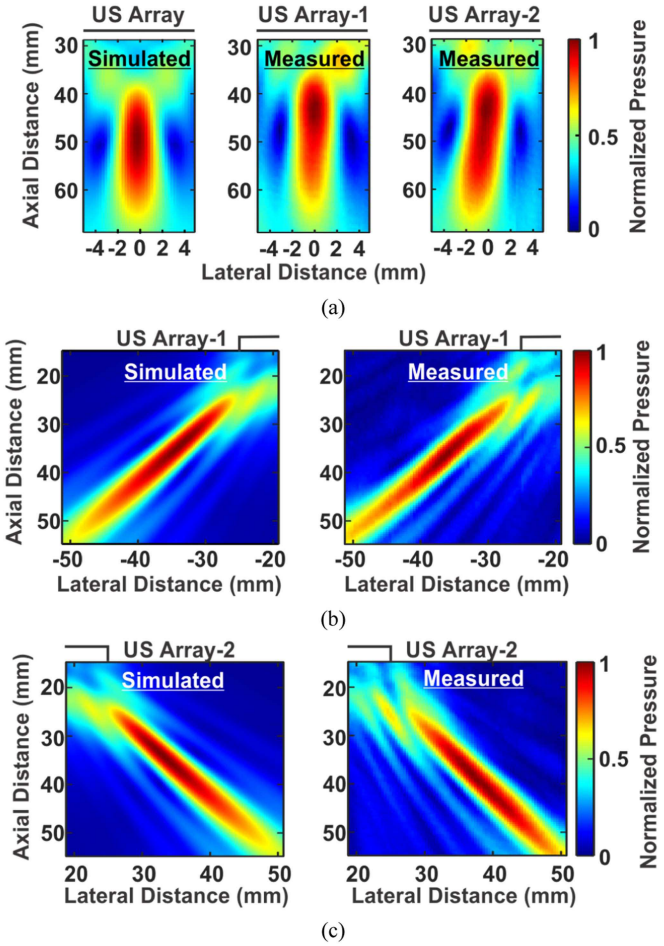

Fig. 10. Comparing the US beam profiles of the array in simulation to those measured for two fabricated arrays for focusing and steering at $F = 50$ mm and (a) $\theta_S = 0°$, (b) $\theta_S = -45°$ (for first array), and (c) $\theta_S = +45°$ (for second array).

Fig. 10 illustrates the simulated and measured US beam profiles of the individual arrays for beam focusing and steering. Fig. 10(a) compares the simulated and measured beam profiles when the beam was focused at $F = 50$ mm ($\theta_S = 0°$). The simulated lateral/axial resolution is 3.1/25.5 mm. The measured lateral/axial resolution is 2.8/24.8 mm and 3.4/26.8 mm, corresponding to measured A_{beam} of 50.4 mm^2 and 61.9 mm^2, for Array-1 and Array-2, respectively. Fig. 10(b) and (c) demonstrate the beam steering capabilities of the fabricated arrays at θ_S of $-45°$ (for Array-1) and $+45°$ (for Array-2) while focusing the beams at $F = 50$ mm, respectively. These results validate the functionality of both arrays and accuracy of the simulations, although there is some discrepancy in pressure distribution and location of maximum peak pressure.

The slight differences between the arrays and among the elements in each array are due to nonidealities and inaccuracies involved in the fabrication, assembly/coating, and measurement of the arrays. This may include any mismatch in the dimensions (e.g., differences in element width due to the dicing inaccuracy), boundary conditions imposed by nonuniform application of the glue and silver epoxy for mechanical reinforcement/attachment, back-side and front-side mechanical loading (likely due to the nonuniformity of the silver epoxy and sylgard-184 layers) and aligning each array with the hydrophone during the beam profile measurement.

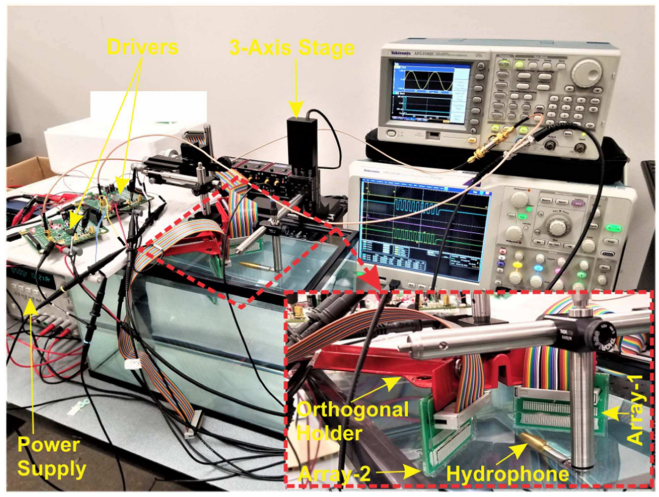

Fig. 11. The experimental setup used to implement and characterize the crossed beams generated by two orthogonal arrays.

B. Crossed-Beam Implementation and Measurements

To implement crossed-beam formation and demonstrate high-resolution focusing with two phased arrays, the experimental setup in Fig. 11 was developed. It includes 1) two 32-channel TX7332EVM drivers modified in both hardware and software to provide two synchronized individual beams by driving two arrays; 2) a function generator providing a 100 MHz external clock for synchronizing two drivers; 3) a high-voltage power supply for the drivers; 4) an automated 3-axis motorized translational stage (MTS50/M-Z8, Thorlabs, Newton, NJ) as described in [26]; 5) an HGL-0085 hydrophone with a 20 dB pre-amplifier (Onda Corp., Sunnyvale, CA) controlled by the automated system with 0.8 μm resolution for accurate capturing of the US pressure output in a water tank; and 6) a digital oscilloscope for acquiring the hydrophone data. All the equipment were synchronized, and the whole measurement process was automated by a custom MATLAB program. To orthogonally position two arrays, a right-angle bracket was used as shown in the inset of Fig. 11.

To form a crossed beam using the phased arrays, they were orthogonally positioned ~ 71 mm apart ($d_C = 71$ mm) with 45° angle with respect to the hydrophone. During the crossed-beam measurements, both arrays were excited with appropriate delays to form their individual beams. Then the hydrophone was moved to estimate the spatial peak pressure position, which should be at the optimum crossing point. The initial lateral line scans were performed to identify if the crossed beam was formed properly. Once the calibration was done, the automated stage was initiated to scan a 16 mm $\times$ 16 mm field with 200 μm steps, maintaining the spatial peak pressure position around the center, which resulted in 2D beam profiles shown in Fig. 12.

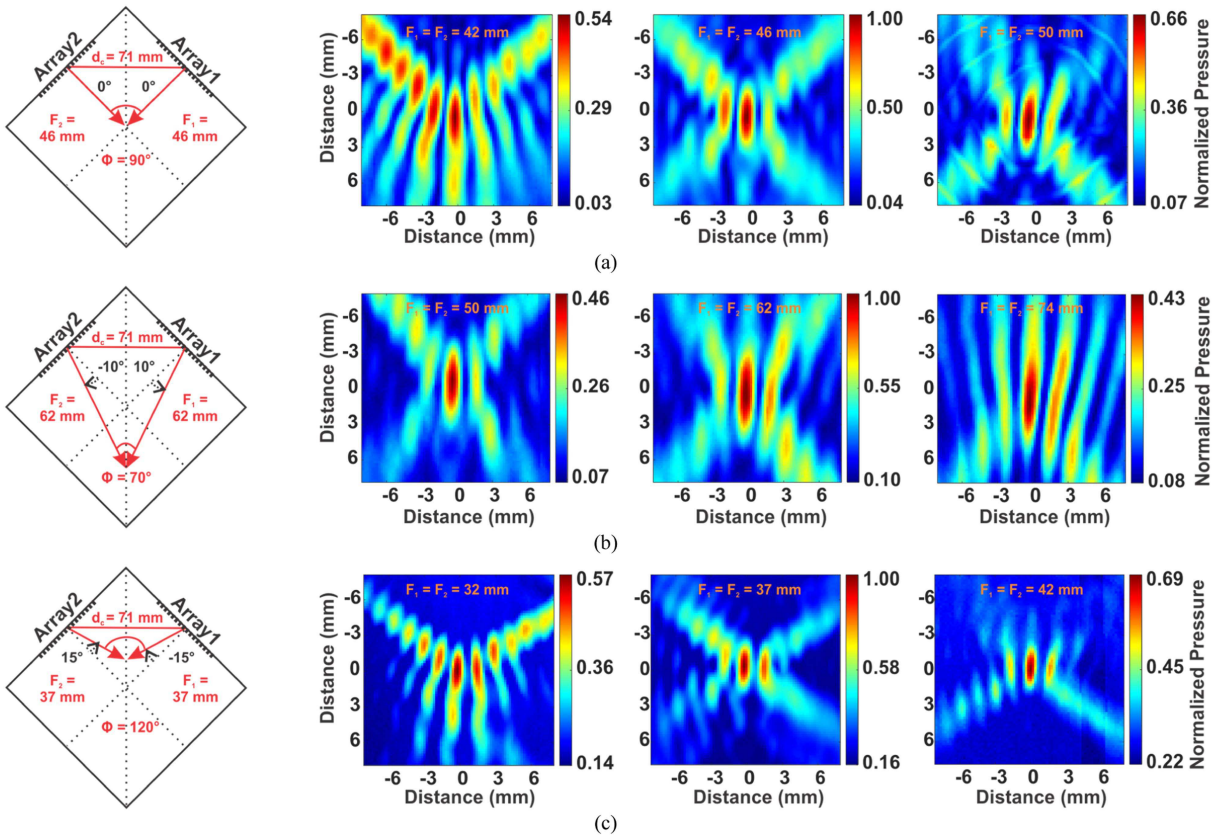

Fig. 12. Measured 2D crossed-beam profiles, formed by crossing two beams generated by two 500 kHz, 32-element arrays, orthogonally positioned with a center-to-center distance of ∼ 71 mm, for crossing angle of (a) $\Phi = 90°$ ($\theta_{S1,2} = 0°$) , (b) $\Phi = 70°$ ($\theta_{S1} = 10°$, $\theta_{S2} = -10°$), and (c) $\Phi = 120°$ ($\theta_{S1} = -15°$, $\theta_{S2} = 15°$). For each Φ, the profile plot in the middle indicates the optimum crossing condition with highest FoM, whereas the left and right ones indicate examples of crossing at non-optimal conditions. The pressures were normalized to the maximum pressure recorded at optimum crossing condition (middle one) of the respective crossing angles.

As discussed in Section II-B, the optimum focal distance was found to be ∼ 35 mm ($F_1 = F_2 = 35$ mm) for $\Phi = 90°$ crossing angle ($\theta_{S1} = \theta_{S2} = 0°$). In measurements (Fig. 12(a) middle), $F_1 = F_2 = F = 46$ mm was found to form the most optimal crossed beam with the highest FoM (main focal spot: lateral/axial resolution = 0.8/3.4 mm; $A_{beam} = 2.18$ mm^2). Compared to the individual array with the measured lateral/axial resolution of 3.4/26.8 mm ($A_{beam} = 61.9$ mm^2; Fig. 10(a)), the crossed beam achieves 4.25/7.88-fold finer lateral/axial resolution with 28.4-fold smaller A_{beam}. To show the sensitivity of the crossed beam to the crossing condition, two more beam profiles with $F = 42$ mm (Fig. 12(a) left) and $F = 50$ mm (Fig. 12(a) right) were also acquired at $\Phi = 90°$. Not only did the beam get distorted with multiple side lobes (resulting in increased A_{beam}), but also a significant reduction in the peak US pressure (46% at $F = 42$ mm and 34% at $F = 50$ mm) was observed in measurements.

Similarly, optimal beam crossing was achieved in measurements at $\Phi = 70°$ ($\theta_{S1} = 10°$, $\theta_{S2} = -10°$; Fig. 12(b)) and 120° ($\theta_{S1} = -15°$, $\theta_{S2} = 15°$; Fig. 12(c). As shown in Fig. 12(b) middle, optimum $F_1 = F_2 = F$ in measurements was found to be 62 mm for $\Phi = 70°$ (different from optimum simulated F of ∼ 45 mm) that resulted in the highest FoM (main focal spot: lateral/axial resolution = 1/5.6 mm; $A_{beam} = 4.28$ mm^2). The two additional measurements at non-optimal $F = 50$ mm (Fig. 12(b) left) and $F = 74$ mm (Fig. 12(b) right) show distorted beams with reduced peak pressure. As shown in Fig. 12(c) middle for $\Phi = 120°$, again, instead of simulated $F_1 = F_2 = F = 30$ mm, the optimum crossing occurred at $F = 37$ mm that resulted in the highest FoM (main focal spot: lateral/axial resolution = 0.8/2.6 mm; $A_{beam} = 1.52$ mm^2). Similarly, two deviated conditions with $F = 32$ (Fig. 12(c) left) and $F = 42$ mm (Fig. 12(c) right) indicate distorted beams and reduced US pressure.

Comparing the simulated crossed beams in Fig. 7 with the measured crossed beams in Fig. 12 (middle plots), two main discrepancies can be observed. First, the required F for optimal crossing was larger in measurements. Second, some small side lobes appeared next to the main focal spot in measurements. These discrepancies could potentially be due to the differences in the beam profiles of the simulated and two fabricated arrays (as also observed in Fig. 10(a)). The US pressure distribution of the simulated beam profile is symmetric and centered at an axial distance of ∼ 50 mm. But the high US pressure zone in the fabricated Array-1 is closer to ∼ 40 mm axial distance, and its pressure output distribution is skewed towards that point as well. The fabricated Array-2 has a similar pattern with an even more skewed pressure profile.

Considering the small side lobes next to each main focal spot, the total measured A_{beam} in Fig. 12(a), (b) and (c) (middle

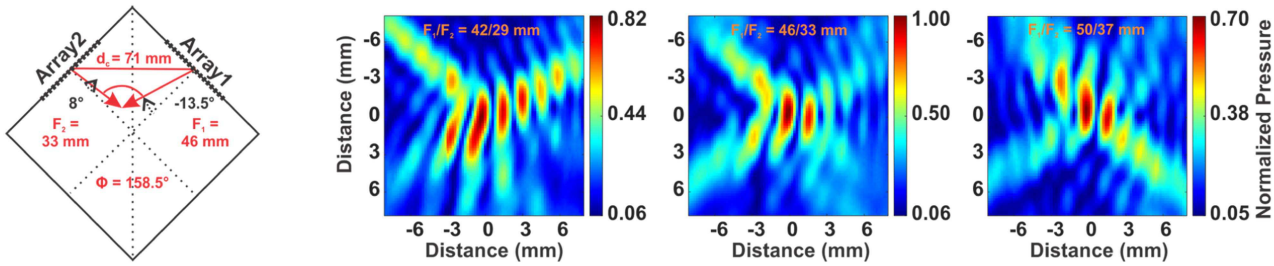

Fig. 13. Measured 2D crossed-beam profiles, formed by crossing two beams from 500 kHz 32-element arrays, orthogonally positioned with a center-to-center distance of ∼ 71 mm, for an arbitrary crossing position with $\theta_{S1} = -13.5°$ and $\theta_{S2} = 8°$. The pressure was normalized to the maximum pressure recorded at optimum crossing condition (middle one).

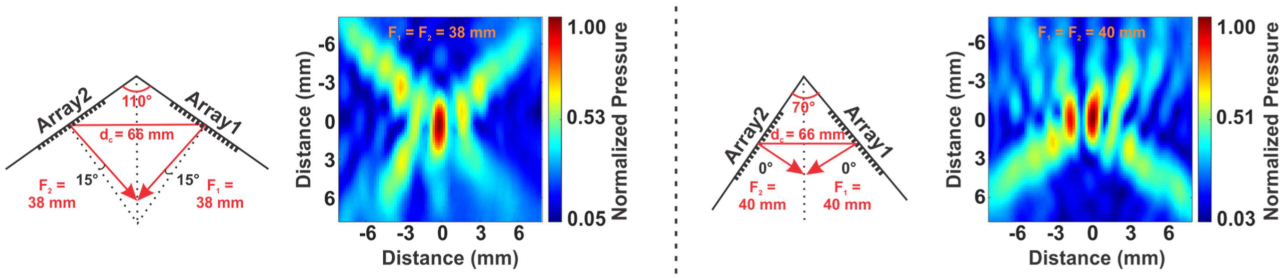

Fig. 14. Measured 2D crossed-beam profiles formed by crossing two beams generated by two 32-element arrays, positioned (d_C of ∼ 66 mm) at relative angles of 110° (left plot; $\theta_{S1} = -15°$, $\theta_{S2} = 15°$) and 70° (right plot; $\theta_{S1} = \theta_{S2} = 0°$).

plots) increase from 2.18 mm^2, 4.28 mm^2, and 1.52 mm^2 (at the main focal spots) to 3.14 mm^2, 5.23 mm^2, and 2.71 mm^2, respectively. Although the total A_{beam} values are slightly higher, they are still significantly lower than the $A_{beam} = 61.9$ mm^2 of the single beam at $F = 50$ mm. These side lobes can potentially be attenuated significantly (similar to simulation results) by fabricating and coating identical arrays with less nonidealities using more advanced fabrication techniques.

The measurements in Fig. 12 show successful beam crossing on the perpendicular bisector of the line connecting the centers of the arrays (Fig. 3(b)). The measurement results in Fig. 13 show the feasibility of beam crossing at an arbitrary point, in which two beams were crossed with $\theta_{S1} = -13.5°$, $\theta_{S2} = 8°$, $F_1 = \sim 40$ mm, and $F_2 = \sim 26$ mm using (1)–(4). A similar initial calibration was performed to find the spatial peak pressure position for scanning a 16×16 mm^2 area with 200 μm resolution. The optimum crossed beam in measurements was found at $F_1 = \sim 46$ mm and $F_2 = \sim 33$ mm (Fig. 13 middle), resulting in $A_{beam} = 1.84$ mm^2 for the main focal spot (total $A_{beam} = 2.89$ mm^2 considering small side lobes). Moreover, two additional beam profiles with $F_1 = \sim 42$ mm and $F_2 = \sim 29$ mm (Fig. 13 left) and $F_1 = \sim 50$ mm and $F_2 = \sim 37$ mm (Fig. 13 right) were measured that achieved 18% and 30% less peak US pressure, respectively, as well as distorted beams with an increased A_{beam}.

IV. Discussion and Future Work

The simulation results in Figs. 4(c), 5(b), and (c) indicate that the crossed-beam formation is possible with two transducers relatively positioned at different angles, and orthogonality of the two transducers (which might not be possible in practical applications) is not a necessity. To verify the crossed-beam formation in a more realistic setup in measurements using two non-orthogonally positioned arrays (orthogonal results were shown in Figs. 12 and 13), the arrays were positioned at 110° and 70° angles with $d_C = 66$ mm, and the delay profiles of the arrays were optimized for proper crossed-beam formation. Fig. 14 shows the measured crossed beam profiles for these conditions, in which the crossed beams were formed properly with the lateral/axial resolution (main lobe) of 0.8/3.4 mm ($F =$ 38 mm) and 0.6/3.2 mm ($F = 40$ mm) for 110° and 70° angles, respectively. These measurements further validate that if the two beams are accurately crossed in space/time, irrespective of the arrays' relative angular position (which mandates different F and θ_S), a crossed beam is properly formed with much higher finer resolution (particularly in the axial direction).

In practical tFUS application, US waves need to propagate through the skull and different tissue layers. We have already studied the effect of the skull on the beam profile of a single 16-element array in [26], observing some distortions in the beam profile shape and a decrease in the peak US pressure output in measurements. To investigate the impact of nonhomogeneous media on the crossed-beam formation, several measurements were conducted in the presence of a ∼ 0.6 mm thick rat skull (size: 40×15 mm^2). The arrays were orthogonally positioned with $\Phi = 90°$, $F_1 = F_2 = F = 46$ mm, and $\theta_{S1} = \theta_{S2} = 0°$ (similar to Fig. 12(a)). To ensure the US waves of the arrays propagate through the relatively smaller rat skull, which was available to us, the skull was placed at two different positions as shown in Fig. 15: 1) On the perpendicular bisector of the line

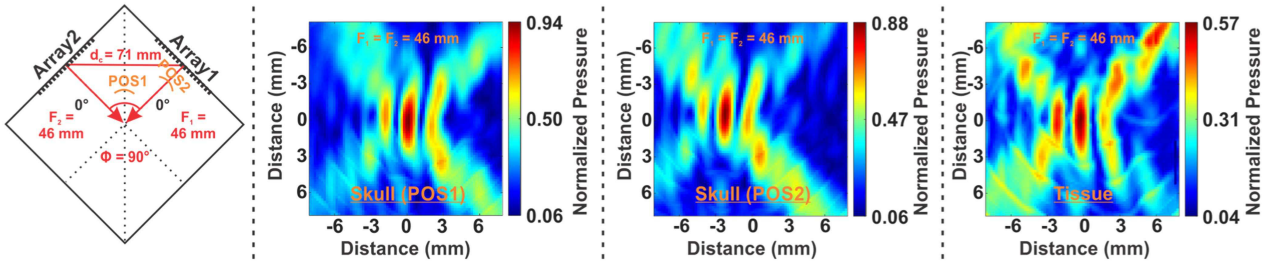

Fig. 15. Measured 2D crossed-beam profiles formed by crossing two beams generated by two 32-element arrays (positioned orthogonally with d_C of ∼ 71 mm) in the presence of a rat skull at two different positions (POS1; POS2) and a large piece of bovine tissue.

TABLE II
CHARACTERISTICS OF ULTRASOUND TRANSDUCERS/ARRAYS COMPARED TO CROSSED-BEAM METHOD FOR ULTRASOUND NEUROMODULATION APPLICATIONS

Characteristics		[7]	[15]	[14]	[21]	[30]	[26]	[27]		This Work	
US Transducer, # Elements (*N*)		Single PZT, 1	Single, 1	Single, 1	CMUT, 32×32	2D, 16×16	1D PZT,16	Single PZT, 1	+90° Crossed	1D PZT, 32	Two 32-el. Arrays; 90° Crossed
Transducer/Array Size (mm)		60 (Dia.)	-	30 (Dia.)	8 × 8	17.5 × 17.5	16.7 × 7.7	19 (Dia.)		50 × 20.5	
Frequency, *f* (kHz)		250	500	270	2000	1000	833.3	5000		555.5	
Focal Distance, *F* (mm)		70	30	30	5	15	12	38.1	38.1	50	46
++Spatial Resolution (mm)	Lateral	7	4.9	3	0.4	1.95	1.6	0.8	1	3.4	0.8
	Axial	47	18	17	2.4	3.14	9	10	1	26.8	3.4
Peak US Pressure (MPa)		-	2.5	1.5	0.575	1.28	1.15	-	(×2.1)	*1.71	*3
US Intensity, I_{SPPA} (W/cm^2)		8 (I_{SPTA})	50	16.6	12.4	-	32.1	0.16	1.12	*78.9	*251.8

+Using two single-element transducers. *Using 150 V peak-peak pulses. ++At the main focal spot.

connecting the array centers and ∼ 12 mm away from the tip of the hydrophone (POS1); 2) At ∼ 10 mm away from the surface of Array-1 (POS2). Fig. 15 shows the measured US profiles with the proper crossed beam formation. The presence of the rat skull resulted in the reduction of the peak US pressure output by 6% (POS1) and 12.3% (POS2), and a slight degradation of the lateral/axial resolution of the main lobe to 0.6/4.2 mm (POS1) and 0.8/3.8 mm (POS2), when compared to the crossed beam profile in Fig. 12(a) (without skull).

Similar crossed-beam measurements were also conducted using a large 9 mm thick piece of bovine tissue (size: 11×5 cm^2). The tissue was placed inside a plastic bag filled with water (to avoid air bubbles) and placed in front of the arrays, fully covering both arrays' surfaces. Fig. 15 also shows the measured crossed beam profile when the tissue was introduced that led to more decrease in the peak US pressure by 42.7% while achieving comparable lateral/axial resolution (the main lobe) of 0.8/4.6 mm. Compared to Fig. 12(a) (no tissue), more lobes with high US pressure appeared in the beam profile in Fig. 15 with tissue. It is worth noting that the delay profiles of the arrays (found in Fig. 12(a)) were not changed when the skull and tissue were introduced to the measurements. Optimizing the delay profiles with some calibration may improve the results and reduce the undesired high-pressure lobes (which is the focus of our future work). Nonetheless, crossed beam formation was still achieved in all these conditions.

Table II benchmarks the crossed-beam method with two phased arrays against relevant US transducers and arrays for neuromodulation applications. The reported single-element transducers and arrays in prior works mostly achieve poor spatial resolution, particularly in the axial direction. The fine axial resolution in [21] and [30] mostly attributes to their large number of elements, high frequency operation, and small focal distance. The orthogonal single-transducer pair in [27] with a crossed beam operated at a high frequency of 5 MHz to achieve a lateral/axial resolution of 0.8/1 mm. In contrast, the two orthogonal 32-element arrays with crossed beam in this work achieved 0.8/3.4 mm lateral/axial resolution (main focal spot) at relatively large (∼ 46 mm) focal distance with a low operation frequency of 555.5 kHz. The main focal beam area is ∼ 28.4-fold smaller than that of the individual 32-element array, demonstrating the significance of beam crossing. The measured peak US pressure and spatial-peak-pulse-average intensity (I_{SPPA}) were as high as 3 MPa (peak-peak) and 251.8 W/cm^2 using 150 V peak-peak pulses.

Some conventional tFUS systems currently utilize an image-guided mechanism for focusing US waves at specific neural targets [8], [31], [32]. Considering the adverse effects of the skull (and different tissue layers) and potential misalignment of the phased arrays for the crossed-beam formation, a similar guiding mechanism is probably required for proper crossing of the beams through electronic control of F and θ_S of each array in neuroscience research and clinical applications in animals and humans. An anatomical image of the subject's head may be utilized in a computational framework to locate the optimal positions of the arrays and correct for skull/tissue aberrations for focusing US crossed beams at a certain brain region. The same transducer arrays may also be used for on-the-fly anatomical imaging of the medium (similar to [19] and [33]) for correcting the US beams. Also, several selectable 1D phased arrays (shown

in Fig. 1) or multiple 2D arrays can ideally be used to cross beams anywhere within a confined volume through electronic beam focusing/steering, regardless of each individual array alignment. This is the main advantage of crossed beam formation using phased arrays. In such a paradigm where the system is scaled up, an optimal phased array pair that provides the maximum FoM for crossed beam formation at a given target can be identified by a computational framework (similar to our simulations in Figs. 4 and 5). These methods and technologies will be developed and demonstrated in our future work.

V. Conclusion

The theoretical foundation of a method, in which two US beams are crossed properly in time/space, was established for high-resolution, large-scale tFUS using phased arrays. Using the k-Wave simulations, the optimal conditions for crossing two beams, generated by two single-element focused (curved) transducers with various curvature and diameter, were studied and then extended to two orthogonal (and coplanar) phased arrays. A method was also proposed for optimizing beam crossing at the right angle and location on the individual beams using k-Wave simulations. It was shown that the optimal crossing angle and location highly depend on the US beam profile of each individual array. Through fabrication of two 555.5 kHz, 32-element phased arrays, successful beam crossing at different locations was demonstrated at a large focal distance of ~ 46 mm, leading to significantly smaller focal spot area. To the best of our knowledge, this is the first implementation of US crossed beams with phased arrays that will potentially open up new avenues for neuroscience research and various clinical applications by providing higher specificity.

References

[1] P. Lewis, R. Thomson, J. Rosenfeld, and P. Fitzgerald, "Brain neuromodulation techniques: A review," *Neuroscientist*, vol. 22, pp. 406–421, May 2016.

[2] W. Tyler, Y. Tufail, M. Finsterwald, M. Tauchmann, E. Olson, and C. Majestic, "Remote excitation of neuronal circuits using low-intensity, low-frequency ultrasound," *PLoS One*, vol. 3, Oct. 2008, Art. no. e3511.

[3] X. Niu, K. Yu, and B. He, "Transcranial focused ultrasound induces sustained synaptic plasticity in rat hippocampus," *Brain Stimulation*, vol. 15, no. 2, pp. 352–359, Mar. 2022.

[4] F. Munoz et al., "Long term study of motivational and cognitive effects of low-intensity focused ultrasound neuromodulation in the dorsal striatum of nonhuman primates," *Brain Stimulation*, vol. 15, no. 2, pp. 360–372, Mar. 2022.

[5] H. Zhou et al., "Wearable ultrasound improves motor function in an MPTP mouse model of Parkinson's disease," *IEEE Trans. Biomed. Eng.*, vol. 66, no. 11, pp. 3006–3013, Nov. 2019.

[6] G. Li et al., "Noninvasive ultrasonic neuromodulation in freely moving mice," *IEEE Trans. Biomed. Eng.*, vol. 66, no. 1, pp. 217–224, Jan. 2019.

[7] W. Lee, P. Croce, R. Margolin, A. Cammalleri, K. Yoon, and S. Yoo, "Transcranial focused ultrasound stimulation of motor cortical areas in freely–moving awake rats," *BioMed Central Neurosci.*, vol. 19, Sep. 2018, Art. no. 57.

[8] W. Lee et al., "Image-guided focused ultrasound-mediated regional brain stimulation in sheep," *Ultrasound Med. Biol.*, vol. 42, no. 2, pp. 459–470, Feb. 2016.

[9] T. Deffieux, Y. Younan, N. Wattiez, M. Tanter, P. Pouget, and J. Aubry, "Low-intensity focused ultrasound modulates monkey visuomotor behavior," *Curr. Biol.*, vol. 23, pp. 2430–2433, Dec. 2013.

[10] E. Mehic, J. Xu, C. Caler, N. Coulson, C. Moritz, and P. Mourad, "Increased anatomical specificity of neuromodulation via modulated focused ultrasound," *PLoS One*, vol. 9, Feb. 2014, Art. no. e86939.

[11] S. Zhu et al., "The updated role of transcranial ultrasound neuromodulation in ischemic stroke: From clinical and basic research," *Front. Cellular Neurosci.*, vol. 16, Feb. 2022, Art. no. 839023.

[12] K. Yu, C. Liu, X. Niu, and B. He, "Transcranial focused ultrasound neuromodulation of voluntary movement-related cortical activity in humans," *IEEE Trans. Biomed. Eng.*, vol. 68, no. 6, pp. 1923–1931, Jun. 2021.

[13] D. Hersh and H. Eisenberg, "Current and future uses of transcranial focused ultrasound in neurosurgery," *J. Neurosurgical Sci.*, vol. 62, pp. 203–213, Nov. 2017.

[14] W. Lee et al., "Transcranial focused ultrasound stimulation of human primary visual cortex," *Sci. Rep.*, vol. 6, pp. 1–12, Sep. 2016.

[15] W. Legon et al., "Transcranial focused ultrasound modulates the activity of primary somatosensory cortex in humans," *Nature Neurosci.*, vol. 17, pp. 322–333, Feb. 2014.

[16] K. Abe and T. Taira, "Focused ultrasound treatment, present and future," *Neurol. Med. Chirurgica*, vol. 57, pp. 386–391, Aug. 2017.

[17] A. Bystritsky and A. Korb, "A review of low-intensity transcranial focused ultrasound for clinical applications," *Curr. Behav. Neurosci. Rep.*, vol. 2, pp. 60–66, Mar. 2015.

[18] H. Kim et al., "Miniature ultrasound ring array transducers for transcranial ultrasound neuromodulation of freely-moving small animals," *Brain Stimulation*, vol. 12, pp. 251–255, Mar. 2019.

[19] G. Li et al., "Imaging-guided dual-target neuromodulation of the mouse brain using array ultrasound," *IEEE Trans. Ultrason. Ferroelect. Freq. Control*, vol. 65, no. 9, pp. 1583–1589, Sep. 2018.

[20] T. Costa, C. Shi, K. Tien, J. Elloian, F. A. Cardoso, and K. L. Shepard, "An integrated 2D ultrasound phased array transmitter in CMOS with pixel pitch-matched beamforming," *IEEE Trans. Biomed. Circuits Syst.*, vol. 15, no. 4, pp. 731–742, Aug. 2021.

[21] C. Seok, O. J. Adelegan, A. O. Biliroğlu, F. Y. Yamaner, and Ö. Oralkan, "A wearable ultrasonic neurostimulator—Part II: A 2D CMUT phased array system with a flip-chip bonded ASIC," *IEEE Trans. Biomed. Circuits Syst.*, vol. 15, no. 4, pp. 705–718, Aug. 2021.

[22] H. Shankar and P. Pagel, "Potential adverse ultrasound-related biological effects a critical review," *Anesthesiology*, vol. 115, pp. 1109–1124, Aug. 2011.

[23] Y. Tufail, A. Yoshihiro, S. Pati, M. Li, and W. Tyler, "Ultrasonic neuromodulation by brain stimulation with transcranial ultrasound," *Nature Protoc.*, vol. 6, no. 9, pp. 1453–1470, 2011.

[24] J. Lu, H. Zou, and J. Greenleaf, "Biomedical ultrasound beam forming," *Ultrasound Med. Biol.*, vol. 20, pp. 403–428, 1994.

[25] H. S. Gougheri, A. Dangi, S.-R. Kothapalli, and M. Kiani, "A Comprehensive study of ultrasound transducer characteristics in microscopic ultrasound neuromodulation," *IEEE Trans. Biomed. Circuits Syst.*, vol. 13, no. 5, pp. 835–847, Oct. 2019.

[26] S. J. Ilham, Z. Kashani, and M. Kiani, "Design and optimization of ultrasound phased arrays for large-scale ultrasound neuromodulation," *IEEE Trans. Biomed. Circuits. Syst.*, vol. 15, no. 6, pp. 1454–1466, Dec. 2021.

[27] S. Kim et al., "Transcranial focused ultrasound stimulation with high spatial resolution," *Brain Stimulation*, vol. 14, pp. 290–300, Mar. 2021.

[28] T. Young, "II. The Bakerian Lecture. on the theory of light and colours," *Philos. Trans. Roy. Soc. London*, vol. 92, pp. 12–48, 1802.

[29] E. Martin, J. Jaros, and B. E. Treeby, "Experimental validation of k-wave: Nonlinear wave propagation in layered, absorbing fluid media," *IEEE Trans. Ultrason. Ferroelect. Freq. Contr.*, vol. 67, no. 1, pp. 81–91, Jan. 2020.

[30] Z. Zhang et al., "New Sm-PMN-PT ceramic-based 2-D array for low-intensity ultrasound therapy application," *IEEE Trans. Ultrason. Ferroelect. Freq. Control*, vol. 67, no. 10, pp. 2085–2094, Oct. 2020.

[31] W. Lee, H. Kim, Y. Jung, I.-U. Song, Y. A. Chung, and S. Yoo, "Image guided transcranial focused ultrasound stimulates human primary somatosensory cortex," *Sci. Rep.*, vol. 5, no. 1, Mar. 2015, Art. no. 8743.

[32] M. Kim, H. Kamimura, S. Lee, C. Aurup, N. Kwon, and E. Konofagou, "Image-guided focused ultrasound modulates electrically evoked motor neuronal activity in the mouse peripheral nervous system in vivo," *J. Neural Eng.*, vol. 17, no. 2, Apr. 2020, Art. no. 026026.

[33] V. Pashaei, P. Dehghanzadeh, G. Enwia, M. Bayat, S. J. A. Majerus, and S. Mandal, "Flexible body-conformal ultrasound patches for image-guided neuromodulation," *IEEE Trans. Biomed. Circuits Syst*, vol. 14, no. 2, pp. 305–318, Apr. 2020.

Sheikh Jawad Ilham (Student Member, IEEE) was born in Bangladesh in 1991. He received the B.Sc. degree in electrical and electronic engineering from the Bangladesh University of Engineering and Technology, Dhaka, Bangladesh, and the M.Sc. degree in biomedical engineering from the University of Connecticut, Mansfield, CT, USA, in 2018. He conducted research on ultrasound neuromodulation on animal models during his master's studies. In 2019, he joined Integrated Circuits and Systems Laboratory, Pennsylvania State University, State College, PA, USA, as a Ph.D. student. His research interests include analog and mixed mode circuits and implantable systems development for various biomedical applications (both therapeutic and diagnostic) with a special focus on ultrasound phased array systems.

Mehdi Kiani (Senior Member, IEEE) received the B.S. degree from Shiraz University, Shiraz, Iran, the M.S. degree from the Sharif University of Technology, Tehran, Iran, in 2005 and 2008, respectively, and the second M.S. and Ph.D. degrees in electrical and computer engineering from the Georgia Institute of Technology, Atlanta, GA, USA, in 2012 and 2013, respectively. In 2014, he joined the Faculty of the School of Electrical Engineering and Computer Science, Pennsylvania State University, State College, PA, USA. His research interests include the multidisciplinary areas of analog, mixed-signal, and power-management integrated circuits, wireless implantable medical devices, neural interfaces, and ultrasound-based medical systems. He was the recipient of 2020 NSF CAREER Award. He is currently an Associate Editor of IEEE TRANSACTIONS ON BIOMEDICAL CIRCUITS AND SYSTEMS and IEEE TRANSACTIONS ON BIOMEDICAL ENGINEERING. He is currently the Technical Program Committee (TPC) Member of the IEEE International Solid-State Circuits Conference. He also served as the TPC Member of IEEE Custom Integrated Circuits Conference and IEEE Sensors Conference.